Supplement of Atmos. Chem. Phys., 23, 13883–13909, 2023
https://doi.org/10.5194/acp-23-13883-2023-supplement

Atmospheric Chemistry and Physics
Open Access
EGU

Supplement of

Mediterranean tropical-like cyclone forecasts and analysis using the ECMWF ensemble forecasting system with physical parameterization perturbations

Miriam Saraceni et al.

Correspondence to: Miriam Saraceni (miriam.saraceni@unipg.it)

In this supporting information, in Section S1 we explain all the perturbed parameters of the Stochastically Perturbed Parameterization (SPP), with a brief description of each parameterization scheme and a small description of how the parameters are perturbed in the SPP scheme. Then, some additional Figures are reported. In **Figure S1** we provide the ensemble standard deviation for each experiment for the daily accumulated precipitation for the corresponding dates in the main text to give a complete analysis and show where there is more uncertainty in the ensemble forecast simulation. In **Figure S2** the Root Mean Squared Error (RMSE) is provided as it changes for increasing starting date for the daily maximum precipitation, to assess how it is decreasing with increasing starting dates at least for Ianos and Zorbas.

Figure S3 and **Figure S4** represent the presence of a deep upper tropospheric trough, cut off from the large-scale circulation and intruding into the Mediterranean area, in the operational analysis, and the ensemble simulations. In these Figures, the 500 hPa Geopotential Height (m), temperature (K), and wind (m/s) are reported in relation to the mean sea level pressure field (hPa). The Figures show that While for Ianos and Zorbas, the presence of the cut-off low is well simulated by the ensemble experiments (Figure SS4a to d), the occurrence of the double cut-off in Trixie is accompanied, in ensemble simulations, by the disappearance of the low that sustained the cyclone, as it is shown in Figure SS4e and f. If one looks at the tracking, all the tracks follow the second cut-off low, because the first one is too weak and disappears before the 29th. This is also linked to the fact that Trixie is not able to be sustained after the 28th-29th in the ensembles and it is not going through the tropical-like phase as in the analysis. This behavior, which is presented here for the simulation starting on the 26th, is consistent also for the other starting dates, with the first cut-off low decreasing intensity and almost disappearing for earlier starting dates. This is reported in **Figure S5**. Indeed **Figure S5** shows the change with increasing starting dates in the deep cut-off low simulation in both the SPP-Conv and the INI experiment to underline the difference within the change of initial conditions.

In **Figure S6** the change in the Potential Vorticity isosurfaces at 2 PVU in the SPP-Conv experiment by increasing starting dates is shown to capture the evolution of the forecast with a better reproduction of the alignment between the upper-level disturbance of the PV field and the heating at 500 hPa. Lastly in **Figure S7** the Total Heat Flux, the sum of the latent heat flux and the sensible heat flux, is shown for each ensemble mean belonging to each experiment, the SPP-Conv, the INI and the SPP ensembles, for the time-step in which the cyclone is entering in its tropical-like phase. This is done to underline the different contributions of surface fluxes in the three medicanes.

S1 Perturbed parameters

The implementation of SPP allows simultaneous perturbations of up to 27 parameters and variables in the deterministic IFS parametrizations. These 27 parameters and variables are reported in Tables S1 - S4.

S1.1 Turbulent diffusion and Boundary layer processes

The turbulent diffusion scheme models vertical heat, momentum, and moisture exchange via sub-grid turbulence. It treats surface layer and higher-altitude transport differently: surface fluxes are computed with first-order K-diffusion based on Monin-Obukhov theory; above, a K-diffusion closure is used universally, with Eddy-Diffusivity Mass-Flux (EDMF) for unstable layers (Köhler et al., 2011). This scheme uses moist conserved variables, predicting total water variance, converting to cloud variables (liquid/ice content, cloud fraction) only for stratocumulus via a total water distribution function. Shallow convection handles convective clouds separately. Unresolved orographical effects are parametrized as momentum sink (drag), with a lower-atmosphere parametrization for small-scale orographic drag (< 5 km) (Beljaars et al., 2004). In stable flow, orographic drag parametrization (which is also called sub-grid orography parameterization) captures low-level blocking due to unresolved orography (blocked flow drag) and gravity wave effects (gravity wave drag) on momentum.

In the turbulence scheme, one of the most important aspects is the turbulent transfer in the boundary layer, with which the atmospheric model knows about the surface boundary condition. Land surfaces tend to be heterogeneous and it is challenging to characterize real terrain in terms of the surface drag that it exerts on the flow, especially in areas with orography. Usually, the Monin Obukhov Similarity is used, which applies to stationary homogeneous conditions. Furthermore, there is much uncertainty regarding the interaction between turbulence and ocean waves. Given that the atmospheric circulation is sensitive to surface drag (Sandu et al., 2016), the chosen parameters of the scheme to be perturbed are related to the surface drag and the

sub-grid orography scheme. Furthermore, the von Kármán constant is perturbed, because several uncertain quantities in the turbulent diffusion scheme are proportional to the von Kármán constant. These are the standard deviation of vertical velocity, which is estimated via an empirical formula, the Obukhov length used to compute the stability functions in the outer layer for surface-driven diffusion, the surface-layer (the level below the lowest model level) mixing length used in the outer layer (the level above the lowest model level) and the cloud-top driven diffusion. It has to be underlined here that the perturbation to the transfer coefficient for momentum over land and over the ocean and the von Kármán constant is changed to be dependent on the type of planetary boundary layer (PBL) type.

Table S1. Perturbed parameter settings for the turbulent diffusion and subgrid orography parameterization. The first column is the parameter identifier, the second is a brief explanation of the role of the parameter in the model. The third column (dist.) indicates the sampled distribution type: LN and N refer to the log-normal and normal distribution, respectively. The fourth column presents the standard deviations of the two underlying Gaussian distributions.

Parameter ID	Role of the parameter	Dist	σ	Scheme
CFM_{OC}	Transfer coefficient for momentum over ocean	LN	0.26, for dry convective PBL 0.33	Mean/Median
CFM_{LA}	Transfer coefficient for momentum over land	LN	0.65, for dry convective PBL 0.78	Mean/Median
$RKAP$	von Kármán constant	LN	0.65, for dry convective PBL 0.26	Mean/Median
$TOFDC$	Coefficient in turbulent orographic form drag scheme	LN	0.78	Mean
$HSDT$	St. dev. of subgrid orography	LN	0.52	Mean
$VDEXC_{LEN}$	Length-scale for vertical mixing in stable boundary layer	LN	1.04	Mean

S1.2 Convection

The moist convection scheme employs a mass-flux approach for deep, shallow, and mid-level convection, determined by cloud depth. Deep convection uses mass flux tied to Convective Available Potential Energy (CAPE) removal. Shallow convection relies on a moist static energy budget, while mid-level convection's mass flux is linked to large-scale vertical velocity. The scheme is described in Tiedtke (1989), then, modifications include an entrainment formulation and a CAPE closure enhancing tropical convection representation (Bechtold et al., 2008, 2014), improving diurnal cycles. In the scheme, the most uncertain processes are the mixing of the cloud with the environment (detrainment and entrainment rates) and the mixing in the sub-cloud layer, the autoconversion in the microphysics of clouds, and the convective momentum transport. The uncertainty of the latter is of particular interest because it depends on the organization of convection and on the fact that it usually acts to reduce the shear, while in the mesoscale convective system, it can also have an opposite effect (Ollinaho et al., 2017). Indeed, the perturbation regards the zonal and meridional convective momentum transport due to shallow and deep convection.

S1.3 Clouds and large scale precipitation processes

The Clouds and large-scale precipitation scheme models them using prognostic equations for cloud liquid, ice, rain, snow water contents, and sub-grid cloud cover. The scheme encompasses cloud and precipitation processes like formation, detrainment from convection, condensation, deposition, evaporation, collection, melting, and freezing. Rooted in Tiedtke (1993), the scheme has evolved with an enhanced representation of mixed-phase clouds and prognostic precipitation (Forbes et al., 2011; Forbes and Tompkins, 2011), even representing ice supersaturation (Tompkins et al., 2007) often found in the upper troposphere. In the scheme, perturbation is added to the different processes of cloud formation, cloud dissipation, rain formation,

Table S2. Perturbed parameter settings for the convection parameterization. The first column is the parameter identifier, the second is a brief explanation of the role of the parameter in the model. The third column (dist.) indicates the sampled distribution type: LN and N refer to the log-normal and normal distribution, respectively. The fourth column presents the standard deviations of the two underlying Gaussian distributions.

Parameter ID	Role of the parameter	Dist	σ	Scheme
$ENTRORG$	Entrainment rate	LN	0.39	Mean
$ENTSHALP$	Shallow entrainment rate	LN	0.39	Mean
$DETRPEN$	Detrainment rate for penetrative convection	LN	0.39	Mean
$RPRCON$	Conversion coefficient cloud to rain	LN	0.52	Mean
$CUDU$	Zonal convective momentum transport, deep convection	N	1.22	Mean
$CUDV$	Meridional convective momentum transport, deep convection	N	1.22	Mean
$CUDUS$	Zonal convective momentum transport, shallow convection	N	1.33	Mean
$CUDVS$	Meridional convective momentum transport, shallow convection	N	1.33	Mean
$RTAU$	Adjustment time-scale in CAPE closure	LN	0.78	Mean
$ENTSTPC1$	Shallow entrainment test parcel entrainment	LN	0.39	Mean

and snow aggregation. The rain evaporation rate, the snow sublimation rate, and the vertical velocity that is used to calculate the adiabatic temperature change for saturation adjustment of condensation and evaporation are perturbed. These perturbations are chosen as they directly change latent heating, which affects atmospheric stability and tropospheric dynamics, particularly in the storm tracks (Attinger et al., 2019, 2021). Indeed, these processes' uncertainty comes from the low understanding of the rain and snow particle size distributions, terminal fall speeds, and particle properties (Boutle and Abel, 2012). Other uncertainties come from the variability of adiabatic heating and cooling, which drives condensation and evaporation. Other perturbations regard the critical relative humidity parameter characterizing the sub-grid heterogeneity of humidity in a grid box and define the relative humidity at which condensation begins to form in the respective grid box.

Table S3. Perturbed parameter settings for the cloud and large-scale precipitation parameterization. The first column is the parameter identifier, the second is a brief explanation of the role of the parameter in the model. The third column (dist.) indicates the sampled distribution type: LN and N refer to the log-normal distribution and the normal distribution, respectively. The fourth column presents the standard deviations of the two underlying Gaussian distributions.

Parameter ID	Role of the parameter	Dist	σ	Scheme
$RAMID$	Relative humidity threshold for the onset of stratiform condensation	LN	0.13	Mean
$RCLDIFF$	Diffusion coefficient for the evaporation of cloud at subgrid cloud edges	LN	1.04	Mean
$RLCRITSNOW$	Cloud ice threshold for autoconversion to snow	LN	0.78	Mean
$RAINEVAP$	Rain evaporation rate	LN	0.65	Mean
$SNOWSUBLIM$	Snow sublimation rate	LN	0.65	Mean
$QSATVERVE$	Vertical velocity used to calculate the adiabatic temperature change for saturation adjustment	LN	0.39	Mean

S1.4 Radiation

The radiation scheme calculates short-wave and long-wave radiative fluxes using predicted temperature, humidity, cloud information, and average monthly aerosol and trace gas climatologies (CO2, O3, CH4, N2O, CFCl3, CF2Cl2). It employs the Rapid Radiation Transfer Model (Mlawer et al., 1997; Iacono et al., 2008), also reproducing cloud interactions using cloud fraction and liquid/ice/snow water content from the cloud scheme via the McICA (Monte Carlo Independent Column Approximation) method (McRad, (Morcrette et al., 2008)). The greatest source of uncertainty in the IFS radiation scheme is the treatment of clouds and aerosols (Morcrette et al., 2008). Indeed, with the use of McICA to represent sub-grid cloud distribution from the cloud fraction and grid box mean cloud water content, uncertainty may arise due to the vertical decorrelation length scale governing the degree to which clouds in adjacent layers overlap, and due to the fractional standard deviation of water content in a given model layer. regarding aerosols, their optical depth for 5 different species is prescribed from a climatology derived from (Tegen et al., 1997). The climatology varies as a function of longitude, latitude, and month. To compute the 3D aerosol distribution, concentrations are assumed to decrease exponentially with height according to a specified scale height for each species. SPP perturbs aerosol optical depth and this scale height independently. Moreover, the other important aspect of parameterization is converting water content to the optical depth of a layer. This is done by parameterizing it as a function of effective radius, which for liquid clouds is calculated as a function of liquid water content (Martin et al., 1994), while ice is a function of temperature. Both parameters are perturbed.

Table S4. Perturbed parameter settings for the radiation parameterization. The first column is the parameter identifier, and the second is a brief explanation of the role of the parameter in the model. The third column (dist.) indicates the sampled distribution type: LN and N refer to the log-normal and normal distribution, respectively. The fourth column presents the standard deviations of the two underlying Gaussian distributions.

Parameter ID	Role of the parameter	Dist	σ	Scheme
$ZDECORR$	Cloud vertical decorrelation height	LN	0.78	Mean
$ZSIGQCW$	Fractional standard deviation of horizontal distribution of water content	LN	0.52	Mean
$ZRADEFF$	Effective radius of cloud water and ice	LN	0.78	Mean
ZHS_{VDAERO}	Scale height of aerosol normal vertical distribution	LN	1.04	Mean
$DELTA_{AERO}$	Optical thickness of aerosol	LN	0.78	Mean

S1.5 Perturbation distribution

If the unperturbed parameters are defined as $\hat{\xi_j}$ (the value of the parameter used in the deterministic forecasts.) for each of the jth parameters, the perturbed parameter is defined as ξ_j, where there are two options of drawing it from either a Gaussian distribution or log-normal distribution, where either the mean or the median is set equal to the unperturbed quantity. SPP samples from a log-normal distribution for most parameters, thus:

$$\xi_j = exp(\Psi_j)\hat{\xi_j}, \quad \Psi_j \sim \mathcal{N}(\mu_j, \sigma_j^2) \tag{1}$$

Here, the perturbations Ψ_j sample a Gaussian distribution with a mean μ_j and a standard deviation σ_j, both determined individually for each perturbed parameter j. The above-mentioned two options considered for determining the mean μ_j are:

1. μ_j = -1/2 σ_j, where the mean of the log-normal distribution of the perturbed parameter ξ_j is equal to the value of the unperturbed parameter $\hat{\xi_j}$;

2. μ_j = -σ_j, where the median of the log-normal distribution of the perturbed parameter ξ_j is equal to the value of the unperturbed parameter $\hat{\xi_j}$;

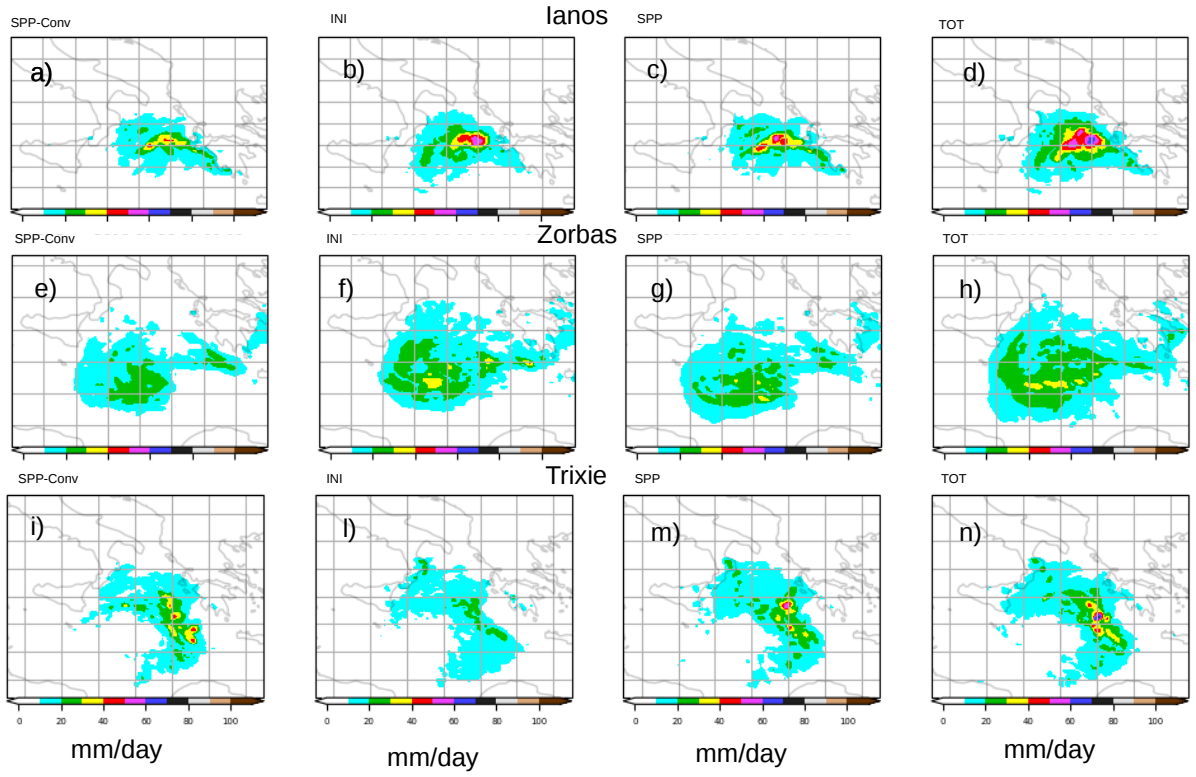

Figure S1. Daily accumulated precipitation (mm/day) standard deviation for the three ensemble experiments ensemble means. For Ianos the 17th is shown in Figures (a), (b), (c) and (d). For Zorbas the 28th is shown in Figures (e), (f), (g) and (h). For Trixie the 28th is shown in Figures (i), (l), (m) and (n). The SPP-Conv ensemble forecast ensemble mean accumulated precipitation standard deviation is reported in the first column, the INI ensemble mean in the second column, the SPP ensemble mean in the third column and the TOT ensemble in the fourth column. For Ianos the experiments starting on the 17th are shown, for Zorbas the ones starting on the 27th and for Trixie the ones starting from the 27th

For most parameters, the log-normal distribution is chosen with the only exception being the zonal and meridional components of the convective momentum transport, which are perturbed with multiplicative noise drawn from a bi-variate normal distribution and they share the same 2D random field. The perturbations $exp(\Psi_j)$ vary in space and time using independent patterns for each parameter j, and for each ensemble member (Figures 1 and 2 of Ollinaho et al. (2017)). The same horizontal pattern is applied to all model levels, in order to maintain physical consistency within a grid column.

S2 Figures

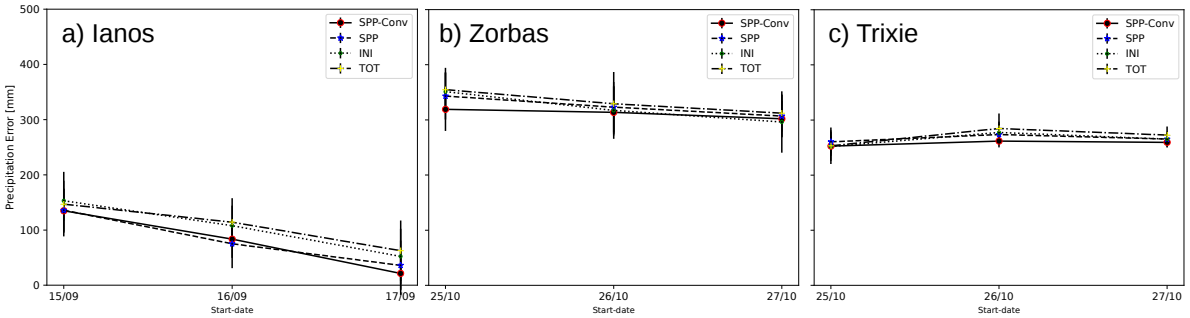

Figure S2. Daily accumulated precipitation (mm/day) root mean squared error between the ensemble mean maximum precipitation and the observed maximum precipitation evolution with increasing starting date for the four ensemble experiments ensemble means. For Ianos in Figure (a) the 17th maximum precipitation is taken, for Zorbas in Figure (b) the 28th maximum precipitation is taken and for Trixie in Figure (c) the 28th maximum precipitation is taken.

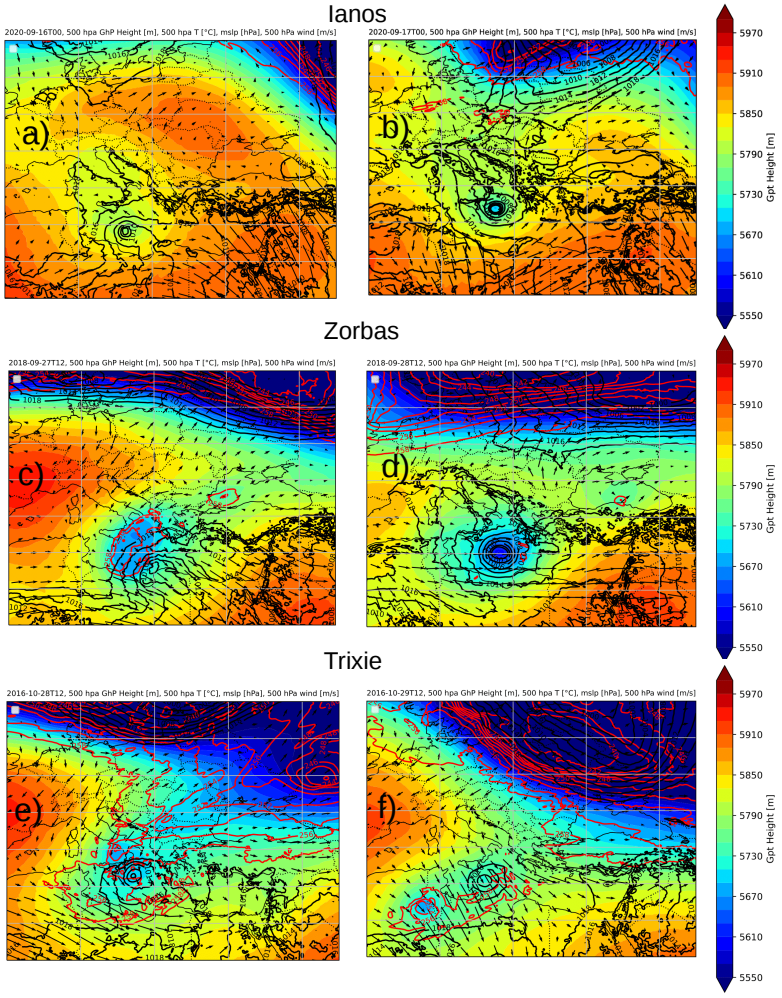

Figure S3. 500 hPa Geopotential height, together with the 500 hPa temperature (red lines) and mean sea level pressure (black lines) for the three medicanes as reproduced by the operational analysis. Ianos synoptic situation is shown for the 16th at 00 UTC in Figure (a) and for the 17th at 00 UTC in Figure (b). Zorbas synoptic situation is shown for the 27th at 12 UTC in Figure (c) and for the 28th at 12 UTC in Figure (d). Trixie synoptic situation is shown for the 28th at 12 UTC in Figure (e) and for the 29th at 12 UTC in Figure (f)

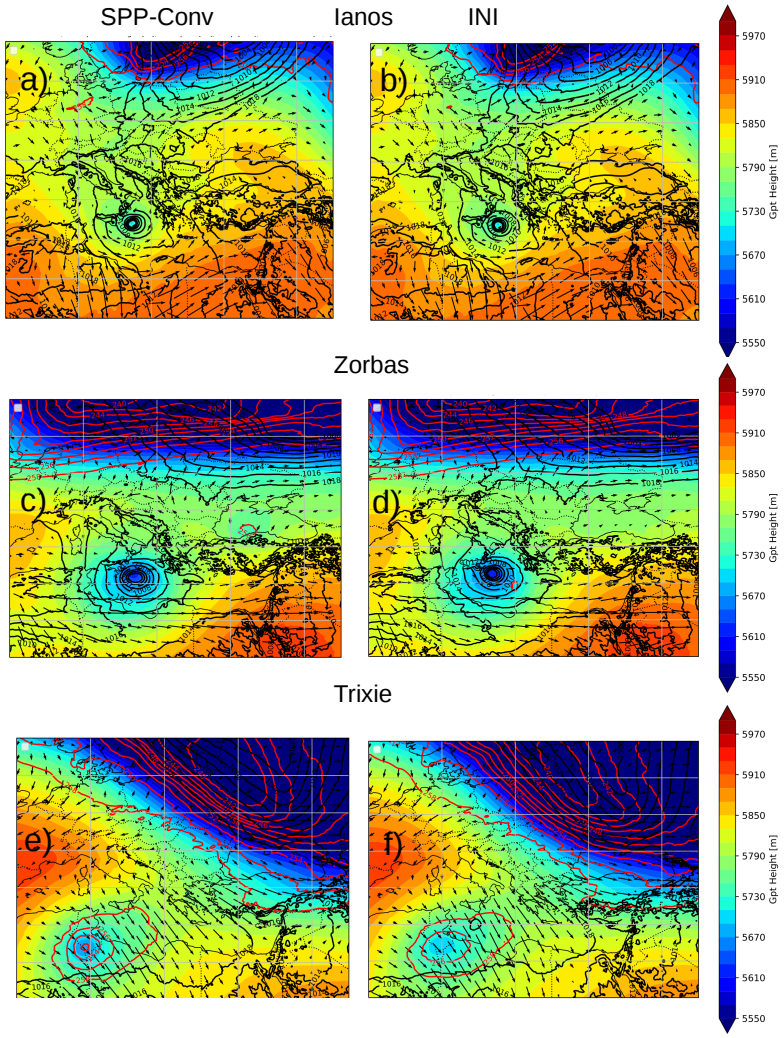

Figure S4. 500 hPa Geopotential height, together with the 500 hPa temperature and mean sea level pressure for the three medicanes as reproduced by the SPP-Conv ensemble in the first column and the INI ensemble in the second column. Ianos synoptic situation is shown for the 17th at 00 UTC in Figures (a) and (b). Zorbas synoptic situation is shown for the 28th at 12 UTC in Figures (c) and (d). Trixie synoptic situation is shown for the 29th at 12 UTC in Figures (e) and (f).

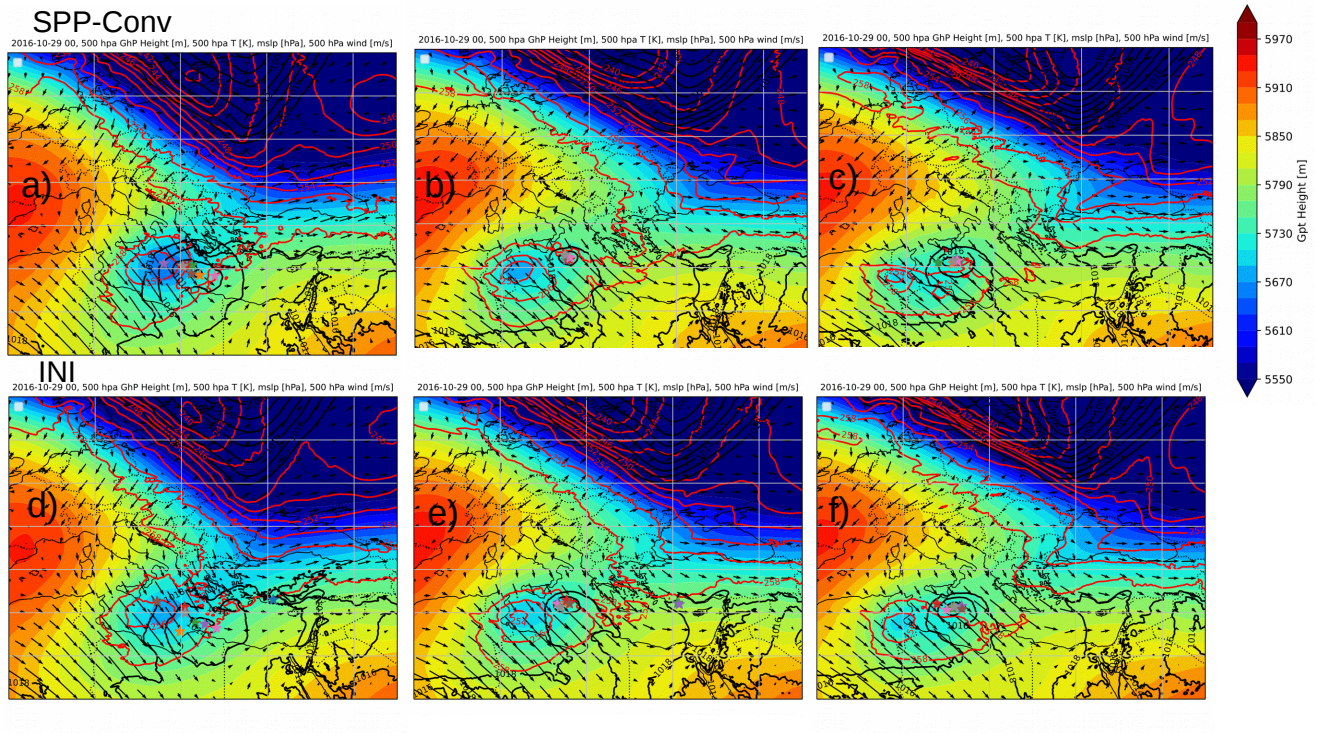

Figure S5. 500 hPa Geopotential height together with the 500 hPa temperature (red lines), mean sea level pressure (black lines), and central position of the ensemble members cyclones (stars) for Trixie cyclones. The 29th at 00 UTC is shown as simulated by the SPP-Conv ensemble for increasing starting dates from the 25th to the 27th in Figures (a), (b) and (c) respectively. The INI ensemble is reported for increasing starting date in Figures (d), (e) and (f) for comparison.

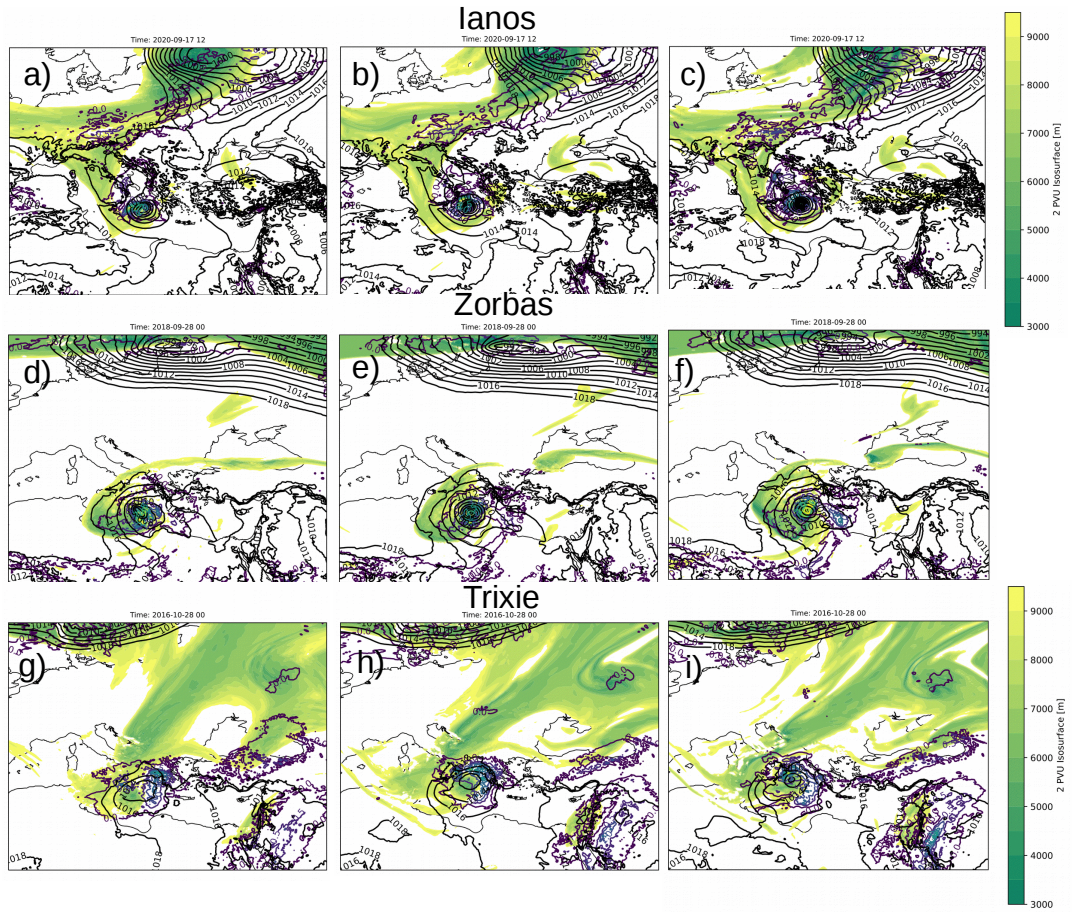

Figure S6. Height of the 2 PVU (PVU = $m^2 K kg^{-1} s^{-1} 10^{-6}$) isosurfaces together with the mean sea level pressure (black lines) and Q1 at 500 hPa for the SPP-Conv ensemble experiment ensemble mean with the increasing starting date. For Ianos the 17th at 12 UTC is reported in Figure (a) as simulated by the experiment starting from the 15th, in (b) as simulated by the experiment starting from the 16th and in (c) as simulated by the experiment starting from the 17th. For Zorbas the 28th at 00 UTC is reported in Figure (d) as simulated by the experiment starting from the 25th, in (e) as simulated by the experiment starting from the 26th and in (f) as simulated by the experiment starting from the 27th. For Trixie the 28th at 00 UTC is reported in Figure (g) as simulated by the experiment starting from the 25th, in (h) as simulated by the experiment starting from the 26th and in (i) as simulated by the experiment starting from the 27th .

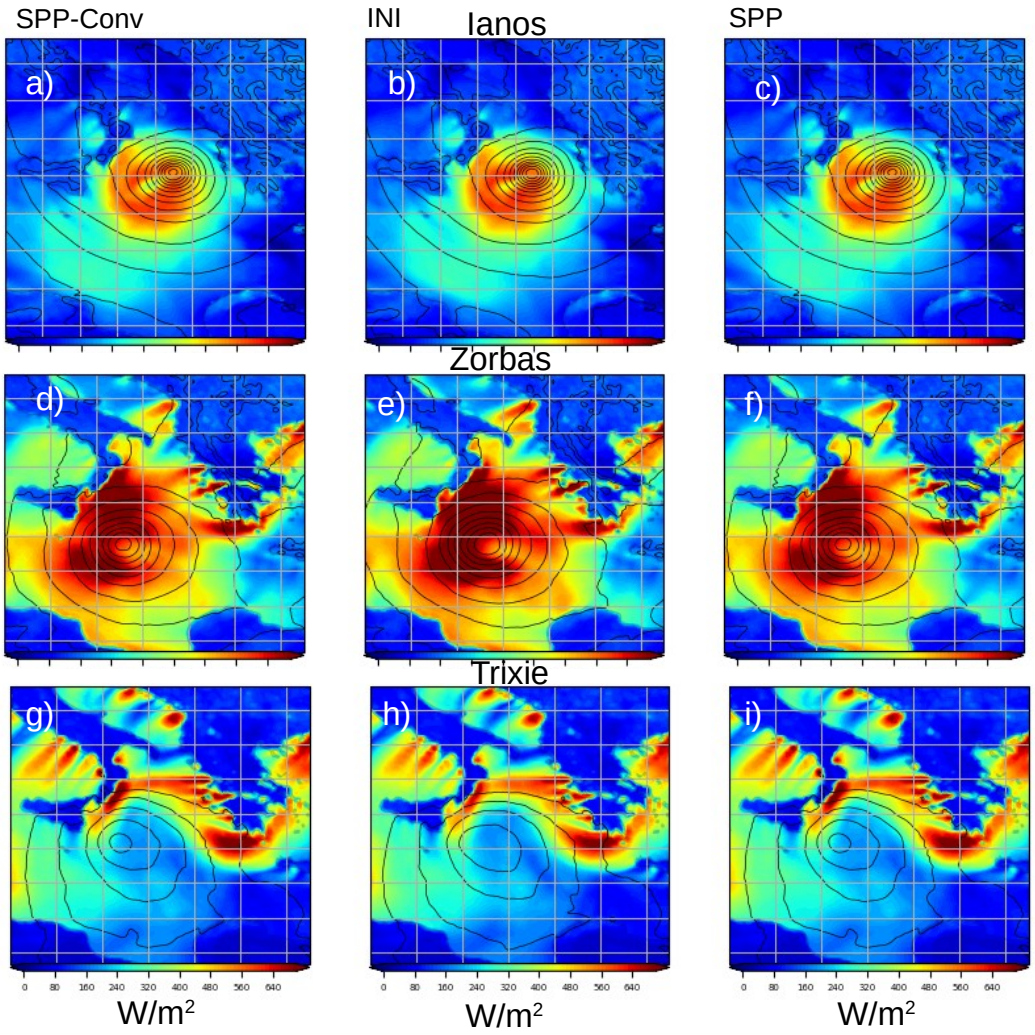

Figure S7. Total surface fluxes (sum of the latent heat flux and the sensible heat flux) (W/m^2) for the three ensemble experiments ensemble means. For Ianos the 17th at 12 UTC is shown in Figures (a), (b) and (c). For Zorbas the 28th at 12 UTC is shown in Figures (d), (e) and (f). For Trixie the 28th at 12 UTC is shown in Figures (g), (h) and (i). the SPP-Conv ensemble forecast ensemble mean is reported in the first column, the SPP ensemble mean in the second column and the INI ensemble mean in the third column. For Ianos the experiments starting on the 17th are shown, for Zorbas the ones starting on the 27th and for Trixie the ones starting from the 27th

References

Attinger, R., Spreitzer, E., Boettcher, M., Forbes, R., Wernli, H., and Joos, H.: Quantifying the role of individual diabatic processes for the formation of PV anomalies in a North Pacific cyclone, Quarterly Journal of the Royal Meteorological Society, 145, 2454–2476, 2019.

Attinger, R., Spreitzer, E., Boettcher, M., Wernli, H., and Joos, H.: Systematic assessment of the diabatic processes that modify low-level potential vorticity in extratropical cyclones, Weather and Climate Dynamics, 2, 1073–1091, 2021.

Bechtold, P., Köhler, M., Jung, T., Doblas-Reyes, F., Leutbecher, M., Rodwell, M. J., Vitart, F., and Balsamo, G.: Advances in simulating atmospheric variability with the ECMWF model: From synoptic to decadal time-scales, Quarterly Journal of the Royal Meteorological Society: A journal of the atmospheric sciences, applied meteorology and physical oceanography, 134, 1337–1351, 2008.

Bechtold, P., Semane, N., Lopez, P., Chaboureau, J.-P., Beljaars, A., and Bormann, N.: Representing equilibrium and nonequilibrium convection in large-scale models, Journal of the Atmospheric Sciences, 71, 734–753, 2014.

Beljaars, A. C., Brown, A. R., and Wood, N.: A new parametrization of turbulent orographic form drag, Quarterly Journal of the Royal Meteorological Society, 130, 1327–1347, 2004.

Boutle, I. and Abel, S.: Microphysical controls on the stratocumulus topped boundary-layer structure during VOCALS-REx, Atmospheric Chemistry and Physics, 12, 2849–2863, 2012.

Forbes, R. and Tompkins, A.: An improved representation of cloud and precipitation, ECMWF Newsletter, 129, 13–18, 2011.

Forbes, R. M., Tompkins, A. M., and Untch, A.: A new prognostic bulk microphysics scheme for the IFS, 2011.

Iacono, M. J., Delamere, J. S., Mlawer, E. J., Shephard, M. W., Clough, S. A., and Collins, W. D.: Radiative forcing by long-lived greenhouse gases: Calculations with the AER radiative transfer models, Journal of Geophysical Research: Atmospheres, 113, 2008.

Köhler, M., Ahlgrimm, M., and Beljaars, A.: Unified treatment of dry convective and stratocumulus-topped boundary layers in the ECMWF model, Quarterly Journal of the Royal Meteorological Society, 137, 43–57, 2011.

Martin, G., Johnson, D., and Spice, A.: The measurement and parameterization of effective radius of droplets in warm stratocumulus clouds, Journal of Atmospheric Sciences, 51, 1823–1842, 1994.

Mlawer, E. J., Taubman, S. J., Brown, P. D., Iacono, M. J., and Clough, S. A.: Radiative transfer for inhomogeneous atmospheres: RRTM, a validated correlated-k model for the longwave, Journal of Geophysical Research: Atmospheres, 102, 16 663–16 682, 1997.

Morcrette, J., Barker, H. W., Cole, J., Iacono, M. J., and Pincus, R.: Impact of a new radiation package, McRad, in the ECMWF Integrated Forecasting System, Monthly weather review, 136, 4773–4798, 2008.

Ollinaho, P., Lock, S.-J., Leutbecher, M., Bechtold, P., Beljaars, A., Bozzo, A., Forbes, R. M., Haiden, T., Hogan, R. J., and Sandu, I.: Towards process-level representation of model uncertainties: stochastically perturbed parametrizations in the ECMWF ensemble, Quarterly Journal of the Royal Meteorological Society, 143, 408–422, 2017.

Sandu, I., Bechtold, P., Beljaars, A., Bozzo, A., Pithan, F., Shepherd, T. G., and Zadra, A.: Impacts of parameterized orographic drag on the N orthern H emisphere winter circulation, Journal of Advances in Modeling Earth Systems, 8, 196–211, 2016.

Tegen, I., Hollrig, P., Chin, M., Fung, I., Jacob, D., and Penner, J.: Contribution of different aerosol species to the global aerosol extinction optical thickness: Estimates from model results, Journal of Geophysical Research: Atmospheres, 102, 23 895–23 915, 1997.

Tiedtke, M.: A comprehensive mass flux scheme for cumulus parameterization in large-scale models, Monthly weather review, 117, 1779–1800, 1989.

Tiedtke, M.: Representation of clouds in large-scale models, Monthly Weather Review, 121, 3040–3061, 1993.

Tompkins, A. M., Gierens, K., and Rädel, G.: Ice supersaturation in the ECMWF integrated forecast system, Quarterly Journal of the Royal Meteorological Society: A journal of the atmospheric sciences, applied meteorology and physical oceanography, 133, 53–63, 2007.